Optics Letters

Integrated silicon nitride time-bin entanglement circuits

Xiang Zhang,[1,2,*] Bryn A. Bell,[1,2] Andri Mahendra,[2,3] Chunle Xiong,[1,2] Philip H. W. Leong,[2,3] and Benjamin J. Eggleton[1,2]

[1]Centre for Ultrahigh Bandwidth Device for Optics Systems (CUDOS), Institute of Photonic and Optical Science (IPOS), School of Physics, University of Sydney, NSW 2006, Australia
[2]The University of Sydney Nano Institute, University of Sydney, NSW 2006, Australia
[3]School of Electrical and Information Engineering, University of Sydney, NSW 2006, Australia
*Corresponding author: b.zhang@physics.usyd.edu.au

Received 29 May 2018; revised 19 June 2018; accepted 19 June 2018; posted 21 June 2018 (Doc. ID 332981); published 16 July 2018

Time-bin entangled photons allow robust entanglement distribution over quantum networks. Integrated photonic circuits positioned at the nodes of a quantum network can perform the important functions of generating highly entangled photons and precisely manipulating their quantum state. In this Letter, we demonstrate time-bin entangled photon generation, noise suppression, wavelength division, and entanglement analysis on a single photonic chip utilizing low-loss double-stripe silicon nitride waveguide structures. Quantum state tomography results show 91 ± 0.7% fidelity compared with the ideal state, indicating that highly entangled photons are generated and analyzed. This work represents a crucial step toward practical quantum networks.

OCIS codes: (270.5565) Quantum communications; (250.5300) Photonic integrated circuits.

https://doi.org/10.1364/OL.43.003469

Entanglement plays an essential role in quantum technologies such as quantum communication, quantum computing, and quantum metrology [1]. In particular for quantum communication, entanglement between remote users is a resource that enables quantum key distribution [2,3], quantum secure direct communication [4–7], quantum teleportation [8], dense coding [9,10], and quantum repeaters [11]. Time-bin entangled photons transmitted through optical fiber are a promising approach for distributing entanglement over long distances. In such an approach, quantum bits (qubits) are encoded onto a photon that can exist in either an early or a late arrival time [2]. These quantum states do not decohere during transmission because photons are naturally well isolated from their environment, and time-bin encoding is highly robust compared to using the polarization or paths of photons [12,13], in terms of stress and temperature fluctuations in fiber. The generation and manipulation of time-bin entanglement usually requires the use of unbalanced interferometers, with a time-delay in one path. Here, the use of integrated photonic chips offers intrinsic phase stability as well as repeatable fabrication of precisely chosen time delays, which are problematic in a fiber or free-space unbalanced interferometer [14]. Meanwhile, the integrated solution imposes stringent requirements on the integration platform. For instance, although the silicon-on-insulator platform has excellent nonlinearity, its propagation loss (3 dB/cm) prohibits the construction of long time delays [15,16]. There have been numerous experiments demonstrating the generation of time-bin entanglement using integrated nonlinear elements to create correlated photon pairs, with the unbalanced interferometers either implemented in fiber or on a separate, linear chip [15,17–19]. However, an integrated photonic chip that includes a photon source and linear circuits will open the possibility of developing a robust, scalable, and cost-efficient quantum network. To the best of our knowledge, this is the first work that combines nonlinear photon-pair generation with linear processing of time-bin entanglement states on a single chip.

In this Letter, we utilize low-loss double-stripe silicon nitride waveguide structures to fabricate an integrated photonic chip that includes entangled pair generation, noise suppression, wavelength division, and entanglement analysis. After carrying out quantum state tomography (QST), a fidelity of 91 ± 0.7% compared with the ideal state indicates highly entangled photons is generated and analyzed in this integrated circuit, demonstrating its potential for practical applications in quantum networks.

Figure 1(a) shows the experimental setup used in this work. A 50 MHz mode-locked laser (MLL) generates 10 ps pump pulses (green) centered at 1552.5 nm. Amplified spontaneous emission (ASE) noise from an internal erbium-doped fiber amplifier (EDFA) is filtered by a band pass filter (BPF) with 0.3 nm full width at half-maximum (FWHM). Pump power and polarization are adjusted by an attenuator (ATT) and a polarization controller (PC), respectively, prior to input to the silicon nitride chip.

The chip utilizes low-loss double-stripe silicon nitride waveguides that support only the transverse electric (TE) mode with 0.2 dB/cm propagation loss [15,16]. <0.1 dB/cm propagation

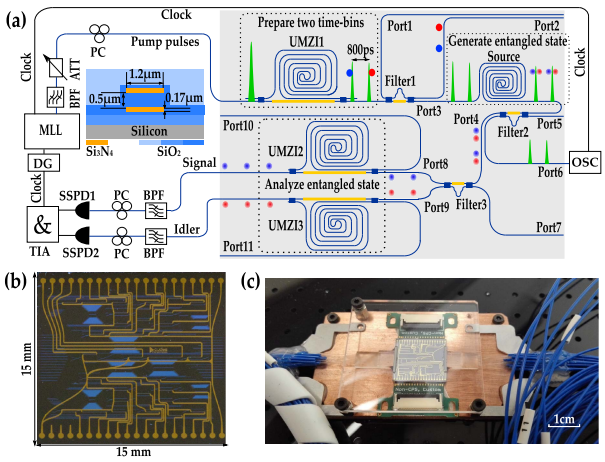

Fig. 1. (a) Experimental setup. MLL, mode-locked laser; BPF, band pass filter; ATT, attenuator; PC, polarization controller; UMZI, unbalanced Mach–Zehnder interferometer; DG, delay generator; OSC, oscilloscope; SSPD, super-conducting single photon detector; TIA, time interval analyzer. Black and blue lines are electronic and optical circuits, respectively. Solid circles are noise photons; blurred circles are entangled photons; gold rectangles are thermal phase shifters. (b) Photo of the bare photonic chip. Yellow lines are electronic connections, and blue lines are the underlying silicon nitride waveguides. (c) Chip after packaging with printed circuit boards (PCBs) and arrays of polarization-maintaining fibers.

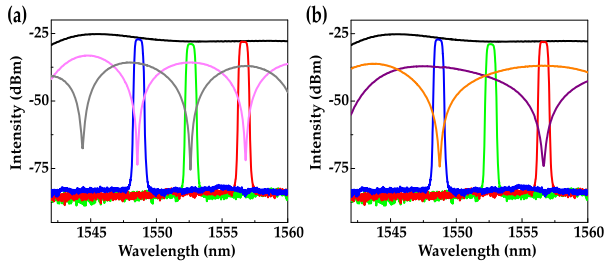

Fig. 2. Spectra of filters 1-3. Black, blue, green, and red lines represent the ASE, signal, pump, and idler spectra, respectively. (a) Spectra of filter 1 (magenta) and filter 2 (gray). (b) Spectrum of filter 3; purple and orange lines represent the signal and idler outputs, respectively. All filters exhibit >30 dB extinction ratios.

loss should be achievable with an optimized fabrication process [20]. Its cross-sectional structure and dimensions are shown as an inset in Fig. 1(a). The schematic of the photonic chip is also illustrated in Fig. 1(a). First, an unbalanced Mach–Zehnder interferometer (UMZI1), with 800 ps time delay between short and long paths, splits each pump pulse into two identical pulses that define two time-bins (early and late). The additional loss (3 dB) introduced by the long arm (14 cm) of UMZI1 is compensated by adjusting the coupling ratio of the input and output couplers so that there is equal power transmitted through each arm [15], and similar for UMZI2 and 3. A thermal phase shifter (gold) in UMZI1 is used to tune the relative phase between early and late pump pulses, θ_p. In the long arm of UMZI1, the strong pump pulses will create noise photons (blue and red circles) by spontaneous four-wave mixing (SFWM) and spontaneous Raman scattering (SpRS). A MZI with a small length imbalance of 176 μm between paths is used to create a filter (filter 1) that transmits the pump pulses but rejects noise at the wavelengths that will be used for the entangled photons. After tuning the phase shifter, the spectrum of filter 1 is shown as the magenta line in Fig. 2(a), and it indicates the spectrum of the signal (blue) and idler (red) where the entangled photons will be created (centered at 1548.5 nm and 1556.5 nm). Comparing with the input spectrum of ASE noise (black), the transmission loss at pump wavelength is around 7 dB. Considering the coupling loss to fiber of 3 dB per facet, this suggests filter 1 has a 1 dB insertion loss. Then a 6.5 cm spiral waveguide is used to generate correlated signal and idler photon pairs via SFWM, a $\chi^{(3)}$ nonlinear process with quadratic dependence on the peak power of the pump pulses. A characterization of photon pair generation in this source is given in Ref. [16]. The photon pairs are created in a coherent superposition state between each time-bin, so their state can be expressed as $(|E\rangle_s|E\rangle_i + e^{2i\theta_p}|L\rangle_s|L\rangle_i)/\sqrt{2}$, where $|E\rangle_x$ and $|L\rangle_x$ represent a photon in the early or late time-bin, respectively, and $x = s, i$ indicates signal and idler wavelengths.

After photon-pair generation, filter 2 with 176 μm length difference is used to separate the pump pulses from the entangled photon pairs. Filter 2's spectrum is shown as the gray line in Fig. 2(a), and its insertion loss at signal and idler are 1 dB and 2 dB, respectively. Pump pulses are sent to an output port (port 6) and monitored by an oscilloscope (OSC). The pump power inside the spiral circuits is estimated by temporarily replacing OSC with a power meter. The measured power of 0.8 mW indicates the average pump power and the peak power inside the spiral are 2.1 mW and 4.2 W, respectively, due to the coupling loss (3 dB) and the propagation loss (1.3 dB). Filter 3 with 88 μm length difference is used to divide the entangled signal and idler photons, with the spectra of the two output ports shown in Fig. 2(b). The insertion loss of filter 3 is around 2 dB. Each filter is particularly designed to perform noise suppression or wavelength demultiplexing based on the characterization of the spiral waveguide in Ref. [16]. The filters have a tuning range of around 800 GHz for their central frequency, using thermal phase shifters. In the measurement, signal and idler are then sent to two separate UMZIs (UMZI2 and 3) with time delays that match UMZI1. These are used to measure and analyze the time-bin qubits. A photon originally in one of two time-bins can arrive at one of three times after passing through an UMZI. A photon previously in the $|E\rangle$ ($|L\rangle$) state can never be detected at the latest (earliest) of the three arrival times. Hence, detecting a photon at the earliest or latest time makes a projective measurement onto the $|E\rangle$ or $|L\rangle$ state. However a photon detected in the middle arrival time could have originated from either time-bin, and so makes a projective measurement onto a superposition state:$(|E\rangle_x + e^{i\theta_x}|L\rangle_x)/\sqrt{2}$, where θ_x is the relative phase between the arms of the UMZI. Each relative phase is controlled by a thermal phase shifter in the corresponding UMZI. The ability to project time-bin qubits onto coherent superposition states makes it possible to verify that they are entangled and to carry out QST.

The photons are coupled off-chip, and residual noise from the pump laser is removed by high isolation (≥60 dB) and low loss (2 dB) BPFs with 0.3 nm FWHM. The polarizations are adjusted by PCs to maximize the detection efficiency of superconducting single-photon detectors (SSPDs) to around 50%.

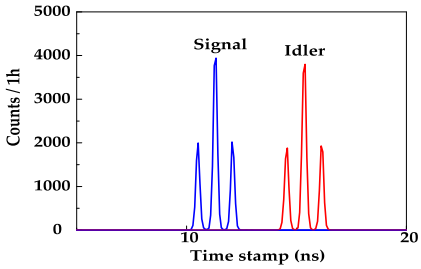

Fig. 3. Histogram of signal and idler arrival times after post-processing time-bin information, relative to the laser clock.

The timing jitter and the dark counts of the SSPDs are <50 ps and around 200 Hz, respectively. A time interval analyzer (TIA, ID800) with 81 ps time resolution is connected to three inputs: signal and idler SSPDs, and the laser clock, which is used for synchronization. The repetition rate of the clock signal is down-converted by a delay generator (DG) to 1 MHz, since the original 50 MHz clock would saturate the TIA. The photonic chip before and after bonding is shown in Figs. 1(b) and 1(c), respectively.

The difference between signal and idler detection times is used to identify photons that originated from the same laser pulse and so constitute an entangled pair; the down-converted clock is sufficient to identify which of the three possible arrival times a given photon was detected in, relative to the original laser clock. An example histogram is given in Fig. 3, showing the relative arrival times. Three peaks are visible for both signal and idler detections. The width of the peaks is due to the combined timing jitter of the SSPDs, the TIA, and the down-converted clock. It can be seen that this jitter is small enough compared to the 800 ps time separation to allow each of the three peaks to be clearly distinguished.

First, two-photon interference is used to calibrate the pump phase θ_p, which is varied while keeping θ_s and θ_i fixed. Figure 4 shows the interference fringe in the two-photon counts, post-selected on both signal and idler arriving in their central histogram peak. A visibility of 88% is obtained from a sinusoidal fit (dashed line). At a maximum in this count rate, $2\theta_p = \theta_s + \theta_i$. Hence, we fix the pump phase at the first maximum, where $V^2 = 64$, and carry out QST by varying θ_s and θ_i, following the method of Ref. [21]. The selected phases of θ_s and θ_i are $\pi/2$ and $-\pi/2$, respectively, in addition to zero for both phases.

The coincidence counts at each specific phase setting have been measured for one hour to suppress statistical uncertainty.

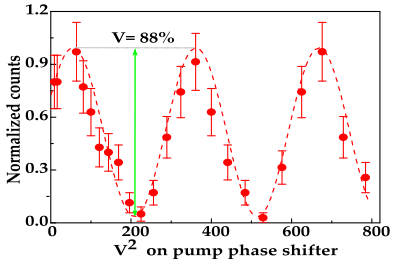

Fig. 4. Two-photon quantum interference with 88% visibility (V); red dots represent the results after post-selecting and count normalization; the dashed line is a sinusoidal fit. Error bars show one standard deviation, assuming Poisson count statistics.

After post-processing, each coincidence count is classified into one of the 16 state projections required for QST [21]. In the time-bin basis, the total coincidence counts where signal and idler arrive in the same time-bin (early or late) are 10.2 k and 11.5 k, compared to <100 for the two combinations where they arrive at different times, demonstrating a high level of correlation. These remaining uncorrelated counts are thought to be noise contributed by detector dark counts, Raman noise, and multi-photon noise. The coincidence counts in the two superposition measurement bases expected to show constructive two-photon interference are around 10–10.5 k. In the other bases, the counts are evenly distributed at around 5–6 k. The average coincidence rate is 7 Hz, which could be improved four-fold by placing detectors at the unused outputs of the signal and idler UMZIs. Each channel has a collection efficiency of around −16 dB, including 3–4 dB from filters 2 and 3, 3 dB from the UMZI, 3–4 dB coupling loss to fiber, 2 dB loss from off-chip filters, 1 dB loss from the PC, and 3 dB loss from detector inefficiency. This suggests an entangled pair generation rate of 45 KHz, around 10^{-3} pairs per pump pulse. Considering its potential applications in quantum networks, further improvements are required to significantly boost the coincidence rate. This could include the use of a ring resonator to enhance the pair generation rate for a given pump power. Other possibilities include integrating low-loss and high-isolation (>95 dB) filters [22], increasing the pump repetition rate [23], and integrating high-efficiency detectors (or number-resolving detectors) [24]. The mode matching to fiber could also be considerably improved using inverse tapers of the output waveguides or polymer mode converters [25].

The density matrix is linearly constructed by the coincidence counts based on the results of the aforementioned state classification, then a maximum likelihood estimation approach is adopted to find a physical density matrix that best fits the experimental results [21,26]. The resulting density matrix has 91 ± 0.7% fidelity compared with the ideal state, as shown

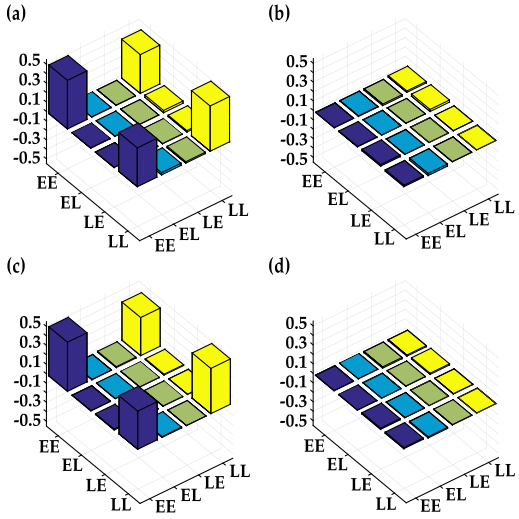

Fig. 5. Density matrix of time-bin entangled photon pairs generated in two samples after maximum likelihood estimation. (a) and (b) show the real and imaginary parts of density matrix in the first sample, respectively. (c) and (d) show the real and imaginary parts of density matrix in the second sample, respectively. EE, EL, LE, and LL represent $|E\rangle_s|E\rangle_i$, $|E\rangle_s|L\rangle_i$, $|L\rangle_s|E\rangle_i$, and $|L\rangle_s|L\rangle_i$, respectively.

in Figs. 5(a) and 5(b). This is consistent with the two-photon interference visibility of 88% measured in Fig. 4, according to Eq. (3) in Ref. [27]. The fidelity is well above the classical threshold of 50%, as well as the 70.7% threshold to violate a Bell's inequality, confirming highly entangled photon pairs are generated and analyzed in this integrated silicon nitride circuit.

The small deviation between the measured state and the ideal state is likely due to the influence of noise sources, such as SpRS noise in the silicon nitride, and errors in the beam-splitter ratios and phase settings on the chip, partially due to the thermal cross-talk between each heater. These problems could be significantly mitigated by cryogenic conditions and a dynamic feedback system. Compared with silicon nanowires, nonlinear photon pair generation in the double-stripe silicon nitride waveguides requires further improvement. Cryogenic temperatures and using a ring resonator instead of spiral waveguides could significantly enhance the generation efficiency and the signal-to-noise-ratio (SNR) [16]. With negligble Raman noise, a 100-fold improvement in count rate should be possible, above which multi-pair events are likely to contribute significant noise. Another strategy to enhance the photon generation rate is to increase the pump repetition rate, where the upper limit is defined by the timing jitter of the detection system, because the minimum delay to distinguish two time-bins is determined by the timing jitter [23].

Apart from stability and scalability, reproducibility is another crucial advantage of CMOS compatible platforms. Another silicon nitride circuit on the same chip with an identical layout has been characterized in this work. After implementing maximum likelihood estimation, $89 \pm 0.6\%$ fidelity is obtained for the second sample, and its density matrix is shown in Figs. 5(c) and 5(d). The 2% fidelity discrepancy between two sources originates from slightly different coupling ratios in UMZIs. The fidelity results of these two chips further confirm the reproducibility of this architecture. In the future, the external filters and SSPDs could also be integrated as high-extinction filters, and near-unity efficiency SSPDs have recently been demonstrated in a silicon nitirde platform [22,28]. This could allow scaling to more complicated functions, e.g., distributed quantum machine learning and multi-photon entangled state generation [29,30]. Here, integrated silicon nitride circuits not only offer a compact and robust platform to generate entangled photons locally, but also allow entangled photons' transmission and analysis between separate photonic chips, such as using ports 10 and 11 shown in Fig. 1 to analyze entangled photons from other nodes in the quantum network.

In this Letter, time-bin entangled photon pairs are generated and analyzed for the first time on a single integrated chip containing silicon nitride photonic circuits. The entangled states are analyzed by QST, and the maximum likelihood estimation indicates highly entangled photons are generated with $91 \pm 0.7\%$ fidelity compared with the ideal state. These results pave the way for a cost-effective and reliable entanglement source for building practical quantum networks.

Funding. Australian Research Council (ARC) (CE110001018, DE1201100226, FL120100029); Huawei Technologies; Indonesia Endowment Fund for Education (LPDP).

Acknowledgment. We would like to thank LioniX for fabricating the silicon nitride chip. We acknowledge funding support from the Australian Research Council (ARC) and Huawei Technologies Inc.

REFERENCES

1. R. Horodecki, P. Horodecki, M. Horodecki, and K. Horodecki, Rev. Mod. Phys. **81**, 865 (2009).
2. I. Marcikic, H. de Riedmatten, W. Tittel, V. Scarani, H. Zbinden, and N. Gisin, Phys. Rev. A **66**, 062308 (2002).
3. A. K. Ekert, Phys. Rev. Lett. **67**, 661 (1991).
4. G. L. Long and X. S. Liu, Phys. Rev. A **65**, 032302 (2002).
5. F.-G. Deng, G. L. Long, and X.-S. Liu, Phys. Rev. A **68**, 042317 (2003).
6. W. Zhang, D.-S. Ding, Y.-B. Sheng, L. Zhou, B.-S. Shi, and G.-C. Guo, Phys. Rev. Lett. **118**, 220501 (2017).
7. F. Zhu, W. Zhang, Y. Sheng, and Y. Huang, Sci. Bull. **62**, 1519 (2017).
8. C. H. Bennett, G. Brassard, R. Jozsa, A. Peres, and W. K. Wootters, Phys. Rev. Lett. **70**, 1895 (1993).
9. C. H. Bennett and S. J. Wiesner, Phys. Rev. Lett. **69**, 2881 (1992).
10. K. Mattle, H. Weinfurter, P. G. Kwiat, and A. Zeilinger, Phys. Rev. Lett. **76**, 4656 (1996).
11. H.-J. Briegel, W. Dür, J. I. Cirac, and P. Zoller, Phys. Rev. Lett. **81**, 5932 (1998).
12. N. Matsuda, H. Le Jeannic, H. Fukuda, T. Tsuchizawa, W. J. Munro, K. Shimizu, K. Yamada, Y. Tokura, and H. Takesue, Sci. Rep. **2**, 817 (2012).
13. J. W. Silverstone, R. Santagati, D. Bonneau, M. J. Strain, M. Sorel, J. L. O'Brien, and M. G. Thompson, Nat. Commun. **6**, 7948 (2015).
14. I. Marcikic, H. de Riedmatten, W. Tittel, H. Zbinden, M. Legré, and N. Gisin, Phys. Rev. Lett. **93**, 180502 (2004).
15. C. Xiong, X. Zhang, A. Mahendra, J. He, D.-Y. Choi, C. J. Chae, D. Marpaung, A. Leinse, R. G. Heideman, M. Hoekman, C. G. H. Roeloffzen, R. M. Oldenbeuving, P. W. L. van Dijk, C. Taddei, P. H. W. Leong, and B. J. Eggleton, Optica **2**, 724 (2015).
16. X. Zhang, Y. Zhang, C. Xiong, and B. J. Eggleton, J. Opt. **18**, 074016 (2016).
17. C. Reimer, M. Kues, P. Roztocki, B. Wetzel, F. Grazioso, B. E. Little, S. T. Chu, T. Johnston, Y. Bromberg, L. Caspani, D. J. Moss, and R. Morandotti, Science **351**, 1176 (2016).
18. Y. H. Li, Z. Y. Zhou, Z. H. Xu, L. X. Xu, B. S. Shi, and G. C. Guo, Phys. Rev. A **94**, 1 (2016).
19. Y.-H. Li, Z.-Y. Zhou, L.-T. Feng, W.-T. Fang, S.-l. Liu, S.-K. Liu, K. Wang, X.-F. Ren, D.-S. Ding, L.-X. Xu, and B.-S. Shi, Phys. Rev. Appl. **7**, 064005 (2017).
20. K. Wörhoff, R. G. Heideman, A. Leinse, and M. Hoekman, Adv. Opt. Technol. **4**, 189 (2015).
21. H. Takesue and Y. Noguchi, Opt. Express **17**, 10976 (2009).
22. A. W. Elshaari, I. E. Zadeh, A. Fognini, M. E. Reimer, D. Dalacu, P. J. Poole, V. Zwiller, and K. D. Jöns, Nat. Commun. **8**, 379 (2017).
23. X. Zhang, B. Bell, M. Pelusi, J. He, W. Geng, Y. Kong, P. Zhang, C. Xiong, and B. J. Eggleton, Appl. Opt. **56**, 8420 (2017).
24. M. D. Eisaman, J. Fan, A. Migdall, and S. V. Polyakov, Rev. Sci. Instrum. **82**, 071101 (2011).
25. P.-I. Dietrich, M. Blaicher, I. Reuter, M. Billah, T. Hoose, A. Hofmann, C. Caer, R. Dangel, B. Offrein, U. Troppenz, M. Moehrle, W. Freude, and C. Koos, Nat. Photonics **12**, 241 (2018).
26. D. F. V. James, P. G. Kwiat, W. J. Munro, and A. G. White, Phys. Rev. A **64**, 052312 (2001).
27. H. de Riedmatten, I. Marcikic, J. A. W. van Houwelingen, W. Tittel, H. Zbinden, and N. Gisin, Phys. Rev. A **71**, 050302 (2005).
28. C. Schuck, W. H. P. Pernice, and H. X. Tang, Appl. Phys. Lett. **102**, 051101 (2013).
29. Y. B. Sheng and L. Zhou, Sci. Bull. **62**, 1025 (2017).
30. J.-W. Pan, Z.-B. Chen, C.-Y. Lu, H. Weinfurter, A. Zeilinger, and M. Żukowski, Rev. Mod. Phys. **84**, 777 (2012).